Electronic Supplementary Material (ESI) for Journal of Materials Chemistry B.

Supplementary Information

Crystal-Reconstructed $BiVO_4$ Semiconductor Photoelectrochemical Sensor for Ultra-Sensitive Tumor Biomarkers Detection

Yang Li,[†] Xianying Dai,[†] Lin He,[‡] Yuyu Bu*[†] and Jin-Ping Ao[†]

[†]Key Laboratory of Wide Band-Gap Semiconductor Materials and Devices, School of Microelectronics, Xidian University, Xi'an, 710071, China

[‡]Shanaxi Provincial Cancer Hospital, Xi'an, 710061, China

1. Fabrication of PEC sensor and PEC detection equipment

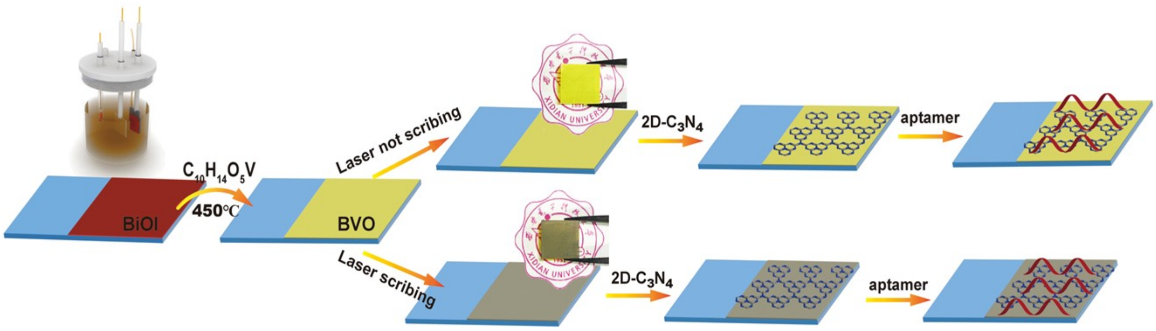

Figure S1. Preparation of the BVO and laser-BVO PEC sensors.

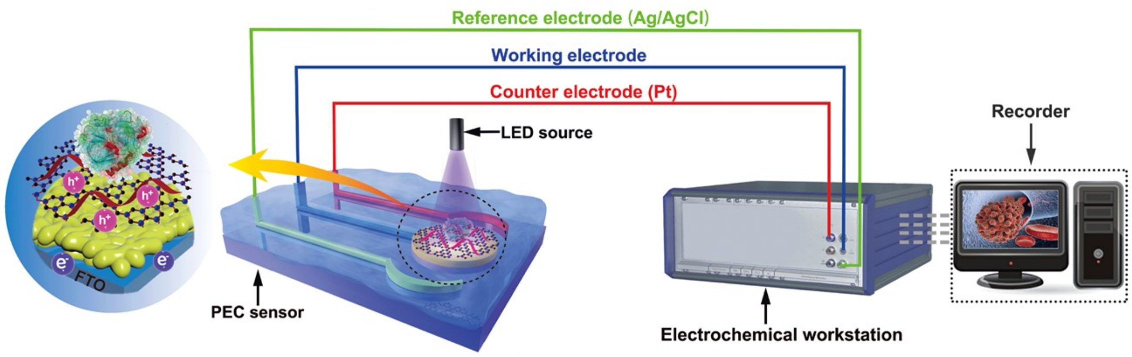

Figure S2. Photoelectrochemical analysis system for PSA specific detection

2. PEC performance of $BiVO_4$ (BVO) and laser treated BVO (laser-BVO) photoanodes.

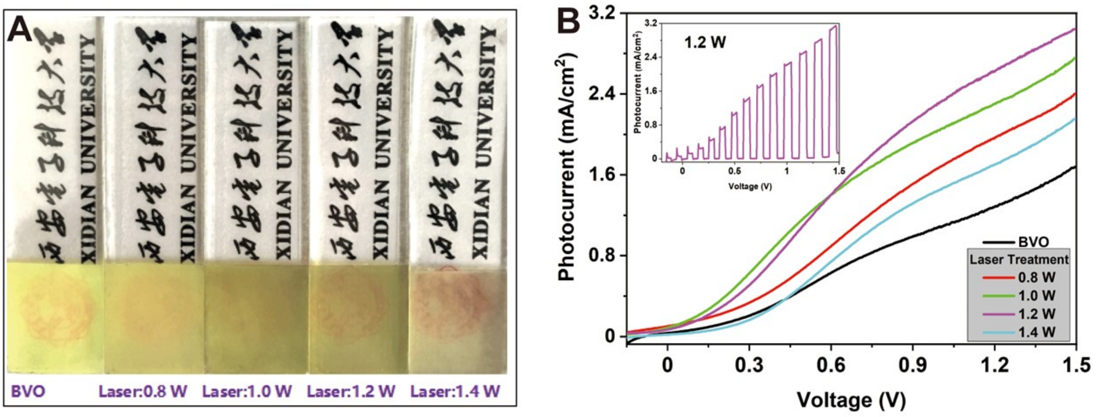

Figure S3. laser treated $BiVO_4$ photoanodes (A)The photographs and (B) photoinduced I-V curves of BVO photoanode and after laser treatment with different power density.

3. Fabrication of BVO/2D-C_3N_4 and laser-BVO/2D-C_3N_4 PEC biosensors

Because there isn't DNA aptamer probes sites on the surface of BVO semiconductor, in order to solve this problem, 2D-C_3N_4 with large π=π electron cloud density was fixed on the surface of BVO and laser-BVO films for PSA DNA aptamer probes fixation. Figure S4A shows the photograph of the 2D-C_3N_4 powder sample and its dispersion liquid. The Faraday-Tyndall effect, which is known as light scattering phenomenon of particles in the suspension, can be clearly observed in the dispersion liquid, indicating that the dispersion contains 2D-C_3N_4 nanosheets. According to the HRTEM results shown in Figure S6B, it exhibits that 2D-C_3N_4 exists as an amorphous 2D sheet-like structure. Figure S4 (C and D) are the HRTEM images of BVO/2D-C_3N_4 and laser-BVO/2D-C_3N_4 after 2D-C_3N_4 modification. We can get the information that 2D-C_3N_4 layer clads closely on the surface of the BVO particle with a thickness of ~5 nm. Figure S4 (E and F) are the photoinduced I-V testing curves of BVO and laser-BVO photoanode after modifying of 2D-C_3N_4 with different amount. The outperformance of photoinduced I-V of BVO and laser-BVO photoanode are achieved by 180 μL and 240 μL 2D-C_3N_4 dispersion modification, respectively. Under this situation, the photogenerated carriers by BVO or laser-BVO can pass through the 2D-C_3N_4 cladding layer (~5 nm) via the tunneling effect, if the photocarriers pass through the 2D-C_3N_4, the reverse recombination probability of free electrons and holes would be suppressed remarkably. Meanwhile, the DNA aptamer probe can be fixed on the surface of BVO/2D-C_3N_4 by the cooperation of π=π bonds on both of 2D-C_3N_4 and DNA aptamer without introduction of other fixation groups. Afterwards, we the important parameters (the incubation time and pH) were optimized. As illustrated in Table S1 and S2, the 30 min and pH=7.4 were selected as the optimal binding time and pH value.

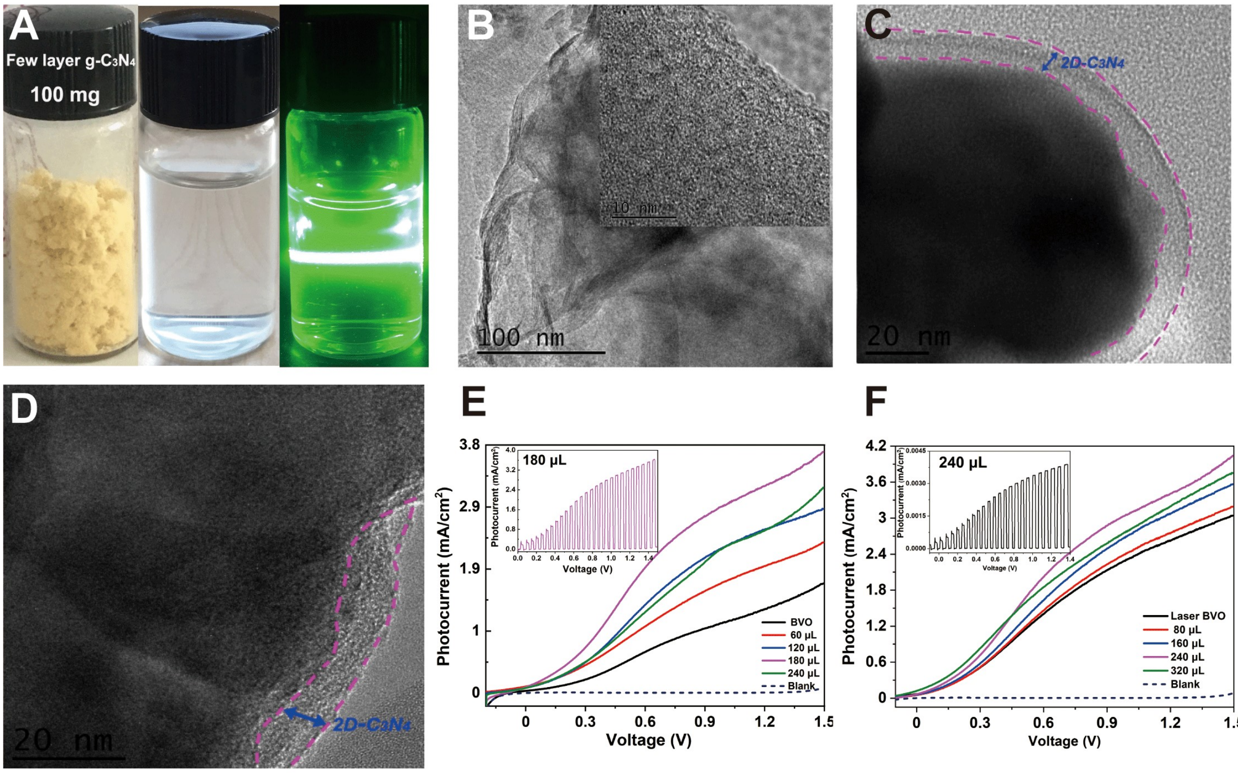

Figure S4. Dispersion, microstructure, and PEC characterizations of 2D-C_3N_4, BVO/2D-C_3N_4 and laser-BVO/2D-C_3N_4 photoanode. (A) Photograph of 2D-C_3N_4 sample and the corresponding dispersion liquid after of exfoliation. (B) and (C) HRTEM of 2D-C_3N_4, BVO/2D-C_3N_4 and laser-2D-C_3N_4. (E) and (F) photoinduced I-V curves of BVO/ 2D-C_3N_4 and laser-BVO/2D-C_3N_4 photoanodes.

Table S1. The optimization of conditions for BVO PEC sensor (the incubation time and pH)

Time (s) ΔCurrent (mA/cm^2) pH	**6.6**	**7.0**	**7.4**	**7.8**	**8.2**
10	**0.02**	**0.04**	**0.04**	**0.14**	**0.03**
20	**0.22**	**0.22**	**0.23**	**0.21**	**0.22**
30	**0.29**	**0.33**	**0.35**	**0.31**	**0.23**
40	**0.29**	**0.33**	**0.34**	**0.35**	**0.33**
50	**0.29**	**0.33**	**0.34**	**0.33**	**0.32**

Table S2. The optimization of conditions for laser-BVO PEC sensor (the incubation time and pH)

Time (s) ΔCurrent (mA/cm^2) pH	**6.6**	**7.0**	**7.4**	**7.8**	**8.2**

10	0.03	0.04	0.04	0.04	0.05
20	0.05	0.07	0.10	0.10	0.08
30	0.07	0.08	0.11	0.10	0.08
40	0.07	0.45	0.11	0.09	0.05
50	0.06	0.45	0.10	0.06	0.05

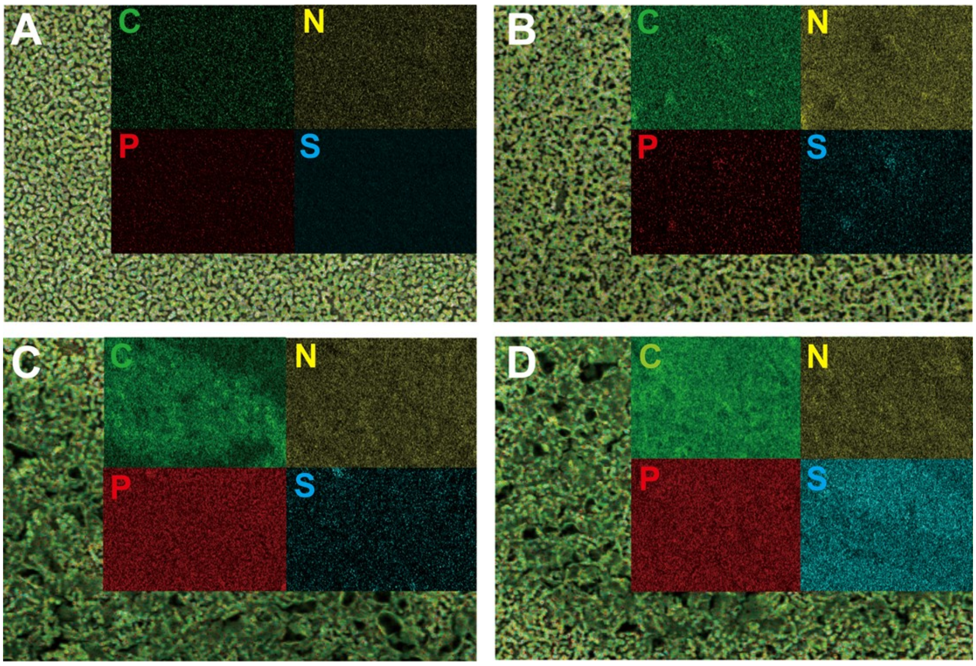

Figure S5. The energy-dispersive X-ray spectroscopy (EDS) mappings (C, N, P, S) of BVO PEC biosensor in different construction process (A) EDS mapping image of BVO thin film. (B) EDS mapping image of BVO /2D-C_3N_4 thin film. (C) EDS mapping image of BVO /2D-C_3N_4/ aptamer thin film. (D) EDS mapping image of BVO /2D-C_3N_4/aptamer/PSA thin film.

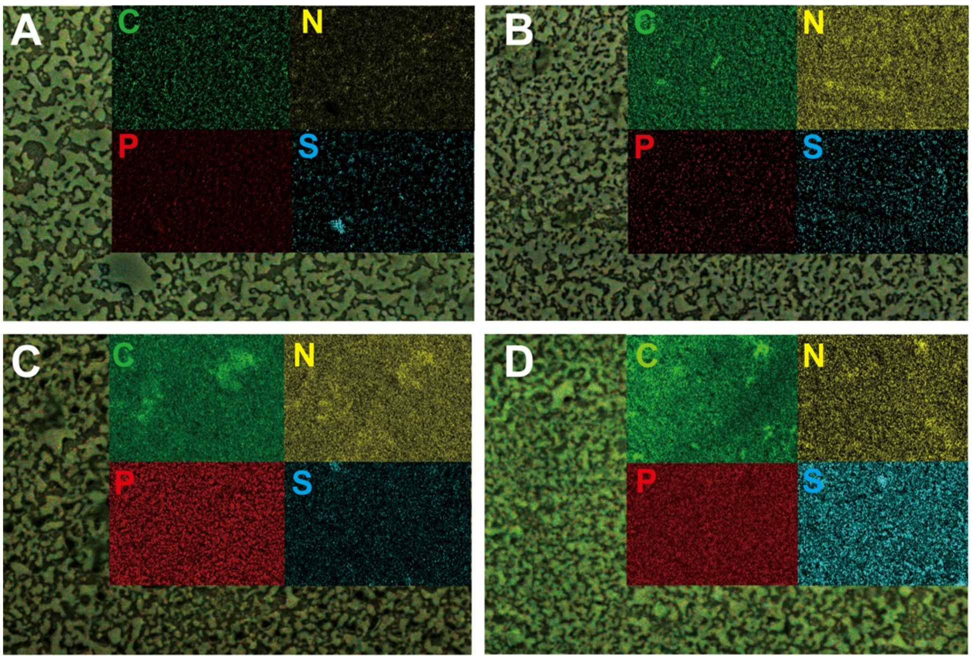

Figure S6. The energy-dispersive X-ray spectroscopy (EDS) mappings (C, N, P, S) of laser-BVO PEC biosensor in different construction process. (A) EDS mapping image of laser-BVO thin film. (B) EDS mapping image of laser-BVO /2D-C_3N_4 thin film. (C) EDS mapping image of laser-BVO /2D-C_3N_4/ aptamer thin film. (D) EDS mapping image of laser-BVO /2D-C_3N_4/aptamer/PSA thin film.

The energy-dispersive X-ray spectroscopy (EDS) mappings (C, N, P, S) of BVO and laser-BVO PEC biosensors in different construction process (in Figure S5 and S6). As shown in Figure.S7B, we can see the C-element and N-element are obviously increased on the BVO film surface after 2D-C_3N_4 modification, indicating the existence of 2D-C_3N_4 (compared to Figure S5A). Figure S5C)shows the mapping of 2D-C_3N_4/BVO, after DNA aptamer modification, the existence of P-element indicate that the aptamer chain was fixed on the 2D-C_3N_4/BVO electrode (because of DNA contains P-element). The mapping of aptamer/2D-C_3N_4/laser-BVO after targeting PSA (in Figure S5D) demonstrate that PSA was specifically binded and aptamer did not fall off the laser-BVO PEC sensor surface (because of PSA contains S-element and P-element did not decrease significantly). By using the similar method to the above, we can demonstrate that laser-BVO PEC is successfully constructed.

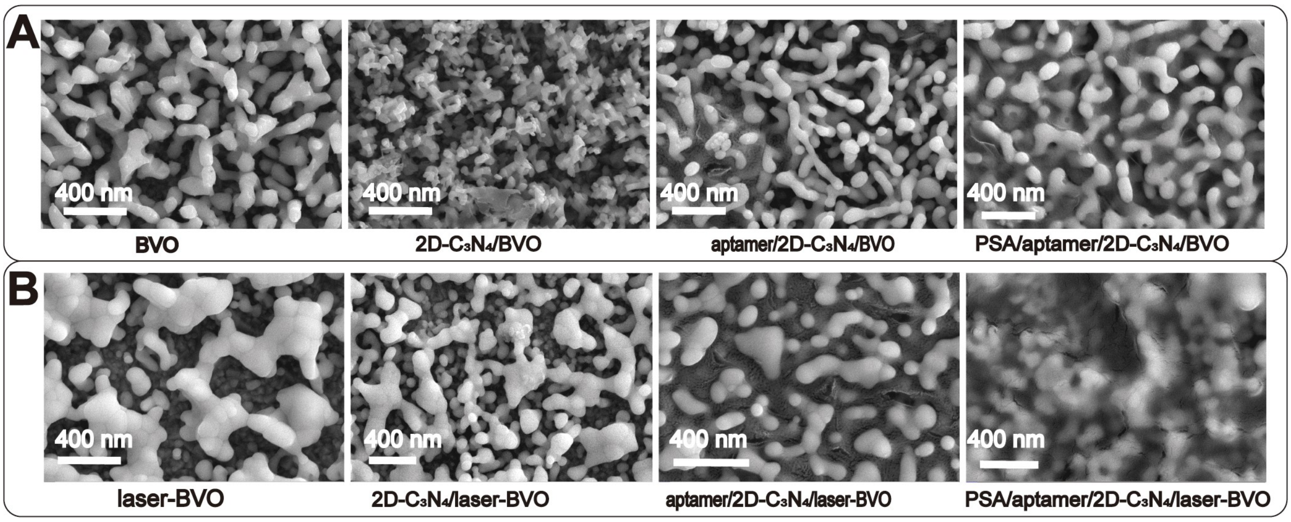

Figure S7. SEM of images of BVO and laser-BVO PEC biosensors in different construction process. (A) BVO PEC biosensor. (B) laser-BVO PEC biosensor.

4. Mechanism of the photocurrent inversion in laser-BVO PEC biosensor by DFT calculation

The calculation models BVO and laser-BVO (oxygen vacancy modified BVO, abb. Vo-BVO) have obtained by cutting and extending along the m-$BiVO_4$ (010) crystal plane (as shown in Figure

S10A). Figure S8 (B and C) present the band structure and the PDOS for both BVO and Vo-BVO crystal models. We can get the information that the band gap structure of the BVO moves to the vacuum level, meanwhile, a doping energy forms on top of the valance band (VB) and overlaps with the Femi-level (E_f) after oxygen vacancy doping in the BVO crystal. Then, the Femi-level of the BVO and Vo-BVO were calculated and the results showed in Figure S8D. The Femi-lever energies of BVO and Vo-BVO locate at 6.88 eV and 5.66 eV, respectively. The upward Femi-lever of Vo-BVO indicates that free electrons are released in the crystal by the breaking of the oxygen-metal bond. More importantly, as shown in Figure S8B, the doping band energy of Vo-BVO is equivalent to the corresponding Femi-lever energy, thus, for the Vo-BVO PEC biosensor, the oxidation energy level of photogenerated holes will decrease to 5.66 eV. Figure S9 (A and B) show the PDOS and electrostatic potentials of BVO/CN and Vo-BVO/CN, we can see that, compared with BVO and Vo-BVO, the lowest occupied surface crystal orbital (LOSCO) of BVO/CN and Vo-BVO/CN shift negatively significantly, the Femi-lever energies of BVO/CN and Vo-BVO/CN are 6.88 eV and 5.66 eV, respectively. The results indicating that the modification of 2D-C_3N_4 will further reduce the oxidation ability of holes. However, Because of the sintering temperature is low and 2D-C_3N_4 layer is about 5 ~10 nm (From Figure S4C and 4D) under this situation, the effect of heterojunction between BVO (or Vo-BVO) and 2D-C_3N_4 is not obvious. the photogenerated carriers by BVO or laser-BVO can pass through the 2D-C_3N_4 cladding layer via the tunneling effect. So we can ignore the effect band structure of 2D-C_3N_4 have on PSA.

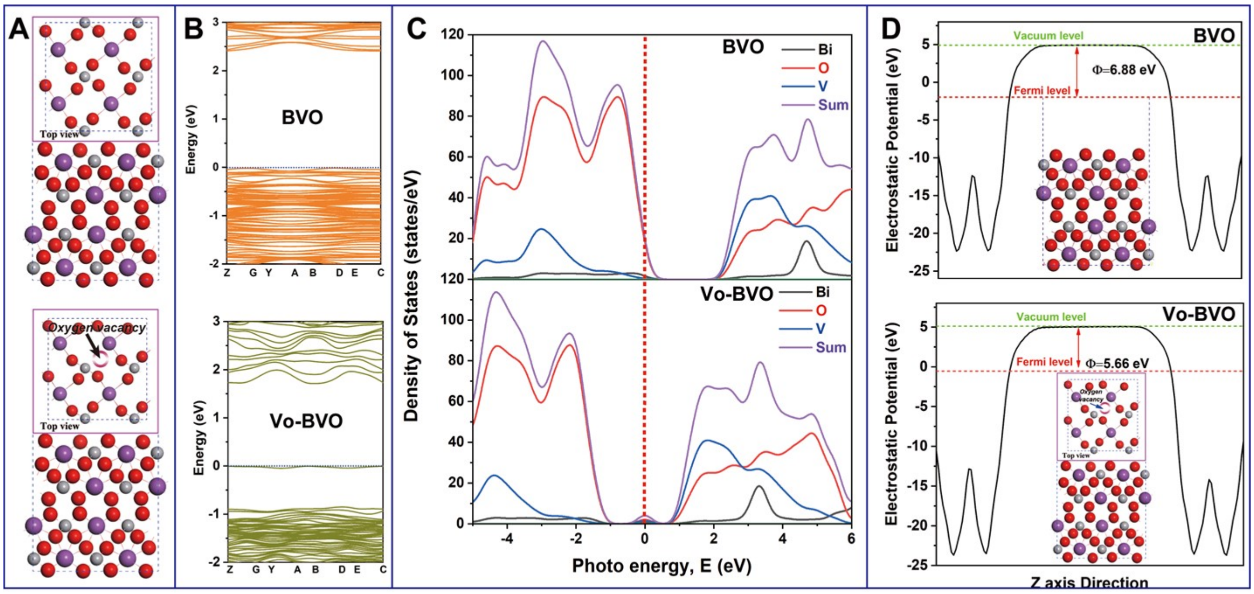

Figure S8. PDOS and electrostatic potentials of BVO and Vo-BVO. (A) Geometry model of BVO (010) and Vo-BVO (010); (B) PDOS of BVO and Vo-BVO; (C) The electrostatic potentials of BVO and Vo-BVO; (D) Fermi level potential of BVO and Vo-BVO.

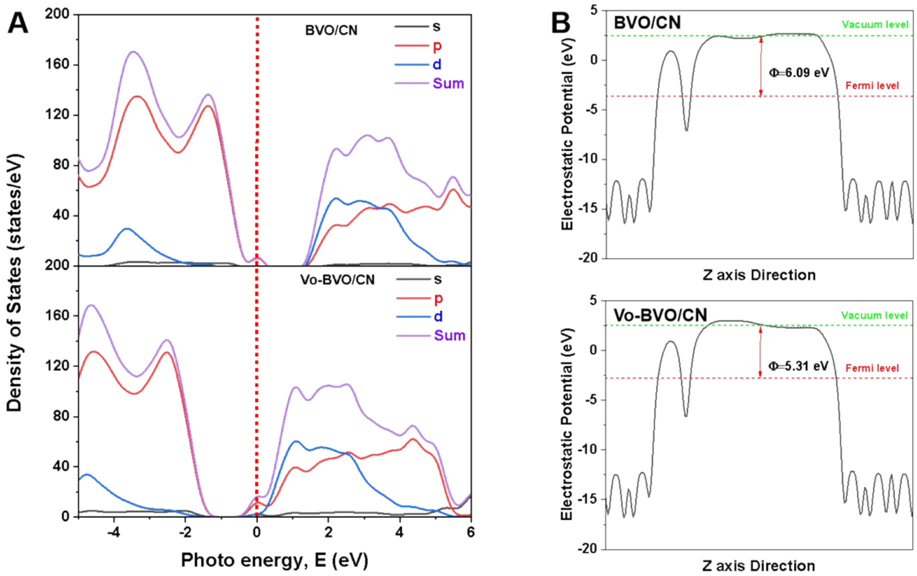

Figure S9. PDOS and electrostatic potentials of BVO/CN and Vo-BVO/CN. (B) PDOS of BVO/CN and Vo-BVO/CN; (C) The electrostatic potentials of BVO/CN and Vo-BVO/CN

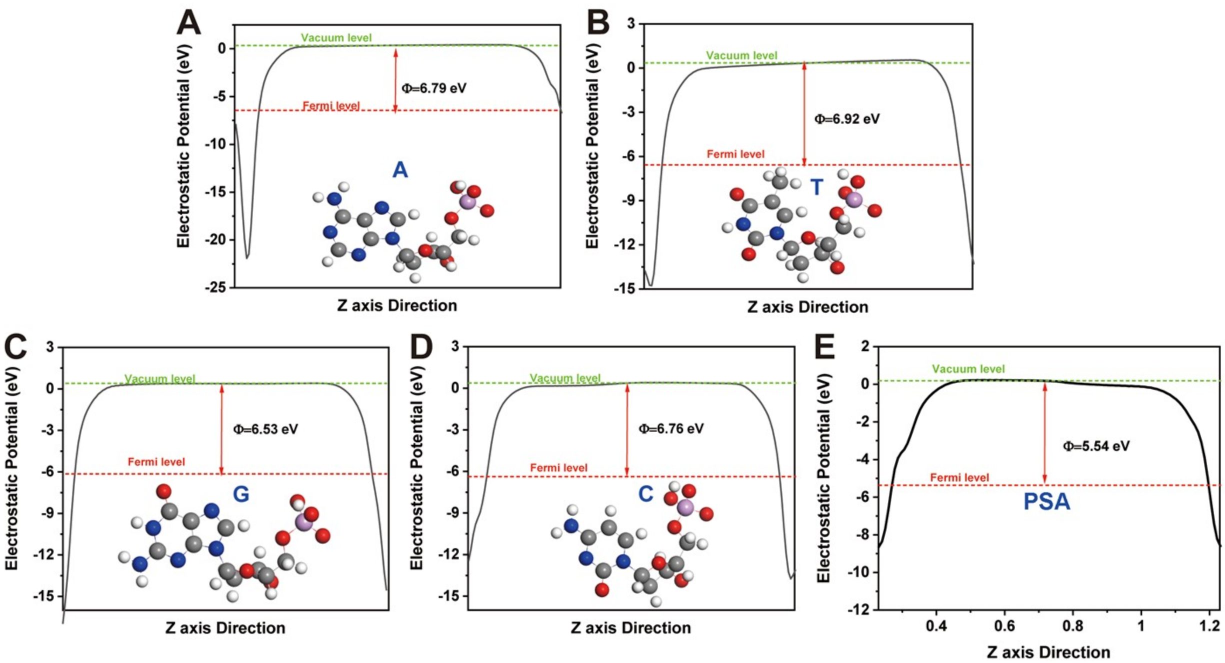

Figure S10. Calculation results of band structure and work function. (**A**) ~ (**E**) The work function of A, T, G, C, PSA respectively.

5. Optimization of the applied potential condition for BVO and laser-BVO PEC biosensor

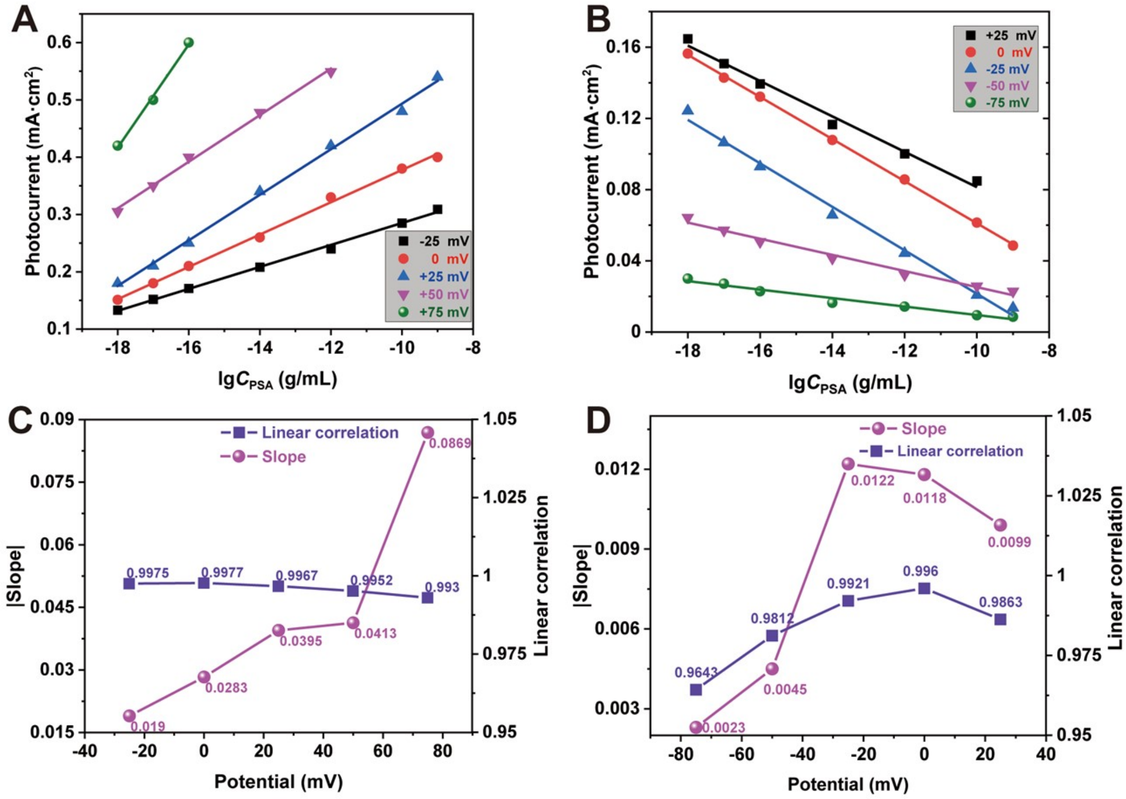

Figure S11. Optimum of the applied bias potential of the BVO and laser-BVO PEC biosensor. (A) and (B) Linear relationship between photocurrent and PSA concentration at different applied bias potential of BVO and laser-BVO PEC biosensor, respectively (vs. Ag/AgCl); (C) and (D) The |slope| and linear correlation of BVO and laser-BVO PEC biosensor at different applied bias potential.

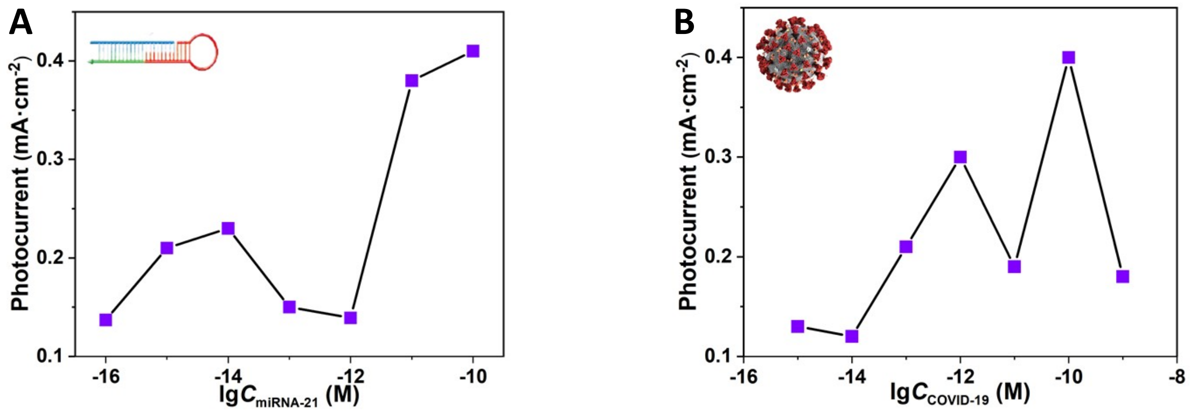

Figure S12. The detection results of BVO PEC biosensor. (A) For miRNA-21 detection；(B) For RdRp-COVID detection.

6. Mechanism of the high sensitivity and resolution rate of the BVO and laser-BVO PEC biosensors

Figure S13A is the optimized model structure of BVO and Vo-BVO crystal models. Compared with BVO, the surface atoms of Vo-BVO significantly shift, mainly because the oxygen atoms near the oxygen vacancies shift and move closer to the oxygen vacancies who take positive electricity. According to the adsorption optimization structure models (Figure S13B) of 2D-C_3N_4 covering on BVO and Vo-BVO crystal models, the surface atoms on Vo-BVO changes more dramatically than BVO after the contact with 2D-C_3N_4, and the fluctuation of 2D-C_3N_4 on Vo-BVO becomes larger than the counterpart also. Based on the above phenomenon, as shown in Figure S15A, the electron cloud overlap at 2D-C_3N_4 and Vo-BVO interface is more obvious, indicating a higher interaction between them. The model structure of the four bases (A, G, T, C) adsorbed by BVO/2D-C_3N_4 and Vo-BVO/2D-C_3N_4 are provided in Figure S13 (C and D). For bases can adsorb on the top of 2D-C_3N_4 layer with a near parallel state, there has letter effect on the atomic structure of 2D-C_3N_4 and BVO after bases adsorption.

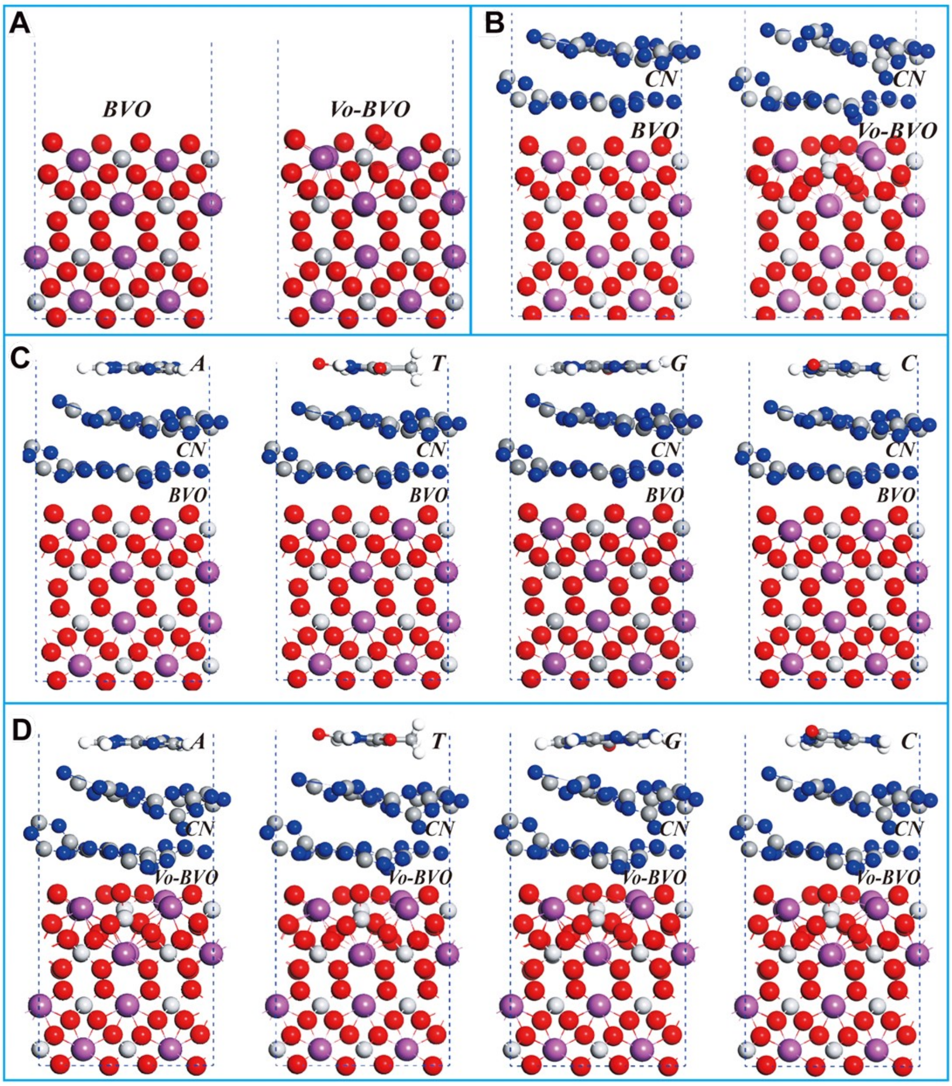

Figure S13. The DFT calculation model. (**A**) BVO and Vo-BVO simulation models after geometric optimization; (**B**) BVO/2D-C_3N_4 and Vo-BVO/2D-C_3N_4 simulation models after geometric optimization; (**C**) BVO/2D-C_3N_4/A, T, G, C simulation models after geometric optimization; (**D**) Vo-BVO /2D-C_3N_4/ A, T, G, C simulation models after geometric optimization.

Table S3. Fitted parameters of the EIS results based on the equivalent circuits.

	BVO		
+25 mV	Samples	R_s	R_{et}
	BVO	25.5 Ω	2.94 kΩ
	2D-C_3N_4	24.1 Ω	1.96 kΩ
	Aptamer	23.8 Ω	2.41 kΩ
	1ng/mL PSA	25.6 Ω	1.50 kΩ
	laser-BVO		
-25 mV	Samples	R_s	R_{et}
	BVO	34.5 Ω	3.38 kΩ
	2D-C_3N_4	39.4 Ω	3.61 kΩ
	Aptamer	31.1 Ω	4.15 kΩ
	1ng/mL PSA	34.2 Ω	4.88 kΩ

Table S4. Calculation data of τ_r, τ_{rec} from CIMPS and CIMVS results, respectively

BVO				
Name	BVO	2D-C_3N_4	aptamer	1 ng/mL PSA
fmin（CIMPS）	54.9 Hz	54.9 Hz	43.2 Hz	33.7 Hz
τ_r	2.90 ms	2.90 ms	3.68 ms	4.73 ms
fmin（CIMVS）	25.9 Hz	25.9 Hz	25.9 Hz	55.1 Hz
τ_{rec}	6.14 ms	6.14 ms	6.14 ms	2.89 ms
Laser-BVO				
Name	Laser-BVO	2D-C_3N_4	aptamer	1 ng/mL PSA
fmin（CIMPS）	173.1 Hz	109.8 Hz	87.5 Hz	69.5 Hz
τ_r	0.92 ms	1.45 ms	1.82 ms	2.29 ms
fmin（CIMVS）	25.9 Hz	25.9 Hz	25.9 Hz	25.9 Hz
τ_{rec}	6.14 ms	6.14 ms	6.14 ms	6.14 ms

7. The long-term storage of the BVO and laser-BVO PEC biosensors, the patient serum samples and patient information

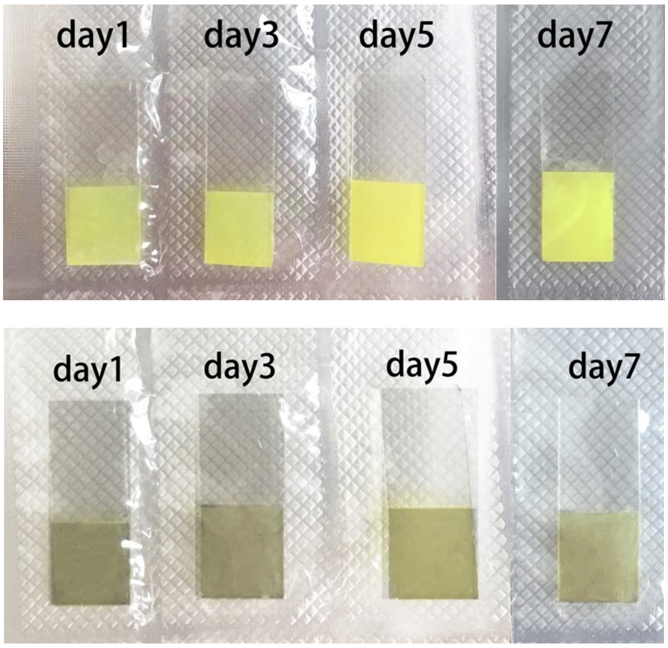

Figure S14. Photograph of sensor samples with sealed state.

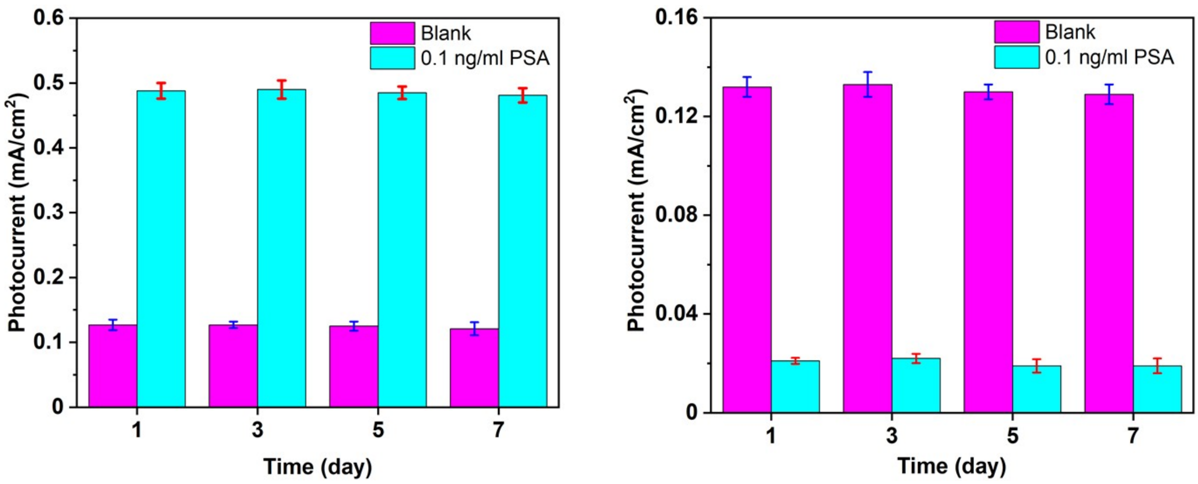

Figure S15. The long-term storage results of the BVO PEC biosensor and laser-BVO biosensor

Table S5. Patients' Information

Patient Code	Year	Gender	Diagnosis results	PSA levels (ng/mL)
1	85	Male	Prostate cancer	0.167
2	65	Male	Secondary malignant tumor of bone	1.12
3	83	Male	Prostate cancer	4.08
4	70	Male	Rectal cancer	10.59

5	**66**	**Male**	**Lung cancer**	**1.03**
6	**64**	**Male**	**Kidney cancer**	**1.32**
7	**56**	**Male**	**Prostate cancer**	**15.86**
8	**73**	**Male**	**Prostate cancer**	**10.58**